Nano Energy 23 (2016) 122–128

Contents lists available at ScienceDirect

Nano Energy

journal homepage: www.elsevier.com/locate/nanoen

Bunchy TiO_2 hierarchical spheres with fast electron transport and large specific surface area for highly efficient dye-sensitized solar cells

Dandan Song [a], Peng Cui [a], Tianyue Wang [a], Bixia Xie [a], Yongjian Jiang [a], Meicheng Li [a,b,*], Yaoyao Li [a], Sheng Du [a], Yue He [a], Zhuohai Liu [a], Joseph Michel Mbebgue [a]

[a] State Key Laboratory of Alternate Electrical Power System with Renewable Energy Sources, School of Renewable Energy, North China Electric Power University, Beijing 102206, China
[b] Chongqing Materials Research Institute, Chongqing 400707, China

ARTICLE INFO

Article history:
Received 12 September 2015
Received in revised form
6 March 2016
Accepted 8 March 2016
Available online 10 March 2016

Keywords:
Nanosheet microspheres
Bunchy sphere
Dye-sensitized solar cells
Photoanode
Efficiency

ABSTRACT

The exploration of TiO_2 nanostructures with fast electron transport and large specific surface area is essential for their applications in solar cells. For this aim, bunchy TiO_2 hierarchical spheres (BS-TiO_2), consisting of multiple TiO_2 microspheres constructed by nanosheets and the 1D TiO_2 nanobelt, were rationally designed and fabricated. BS-TiO_2 enables the much fast charge transport properties in the photoanode (with a long electron diffusion length of 36 μm) and shows large specific surface area (higher than 200 m^2/g), leading to excellent electron collection and light harvesting, which enable the increased conversion efficiency of the dye-sensitized solar cell by 34% for BS-TiO_2 photoanode (7.5%) compared to nanoparticle (P25) photoanode. This work provides an important approach for the rational design of the TiO_2 nanostructures, which also implies the application of the bunchy TiO_2 hierarchical spheres in other type of solar cells, artificial photosynthesis, and other optoelectronic applications.

1. Introduction

Dye-sensitized solar cells (DSCs), with the advantages of high efficiency, low-cost and relatively high stability [1,2], are a photoelectrochemical system with dye-adsorbed porous-structured oxide (typically TiO_2) as the photoanode. As the key component of a DSC, the photoanode governs the electron collection efficiency and light harvesting efficiency, and thus the overall cell conversion efficiency. The light harvesting efficiency, depending on the surface area of electrode materials for dye adsorption, is normally associated with the high porosity and small size of building blocks (e.g., nanoparticles). However, high surface area films consisting of nanocrystalline particles yield high grain boundary densities, which increase the charge carrier recombination through loss of carrier mobility [3]. The rapid charge transport property usually relies on the straight conducting pathways [3–5], such as nanotubes, nanorods, while the dye-adsorption is limited in these films due to the small surface area of these films. Though the trade-off between the light harvesting and the carrier transport is an inevitable and universal problem in DSCs, the solutions have not been well explored.

One promising strategy to solve the problem is to integrate the small sized building blocks into the micro sized architectures. The architectures, such as nanocrystallite aggregates, dendritic spheres, typically exhibit three-dimensional (3D) spherical morphology [6–10]. These TiO_2 architectures can provide large surface areas for dye-loading favored by the small building blocks, and improved electron collection by the reduced defects or grain boundaries inner the spherical architecture. In addition, it has been found that the micro and mesoporous TiO_2 materials also allow the light waves to penetrate deep inside the photoanode and make the photoanode more efficient in light harvesting [11–13]. The DSCs using the photoanodes fabricated from these architectures typically show increased light harvesting compared with traditional P25 or small sized TiO_2 nanoparticles [14]. However, the increase in the cell efficiency is limited or is even lower with the introduction of 3D spherical architecture [15], probably due to the small size of the inner grains in the micro-architectures which is not able to form the built-in potential and increases the recombination with their large surface area.

Substantial research efforts for overcoming the competition between the light harvesting and charge collection have been recently focused on building nanoblocks on the one-dimensional (1D) trunks (e.g., nanorods, nanotubes), i.e., hierarchical architectures [4,5,16]. The electron transport is expected to via the 1D trunks, while the surface nanostructures can increase the surface area for dye-loading [5,16]. In addition, the light scattering can

* Corresponding author at: State Key Laboratory of Alternate Electrical Power System with Renewable Energy Sources, School of Renewable Energy, North China Electric Power University, Beijing 102206, China.
E-mail address: mcli@ncepu.edu.cn (M. Li).

http://dx.doi.org/10.1016/j.nanoen.2016.03.006
2211-2855/

also be enhanced in the hierarchical architectures. However, due to the small surface area of 1D trunks, limited nanoblocks can be built on their surface, which limits the surface area of the hierarchical architecture for dye-loading. For example, with TiO_2 nanosheets deposited on SnO_2 nanotubes, the specific surface area is only increased by a small extent from 70 m^2/g to no more than 85 m^2/g [5]. Therefore, though the DSCs using these kinds of hierarchical architectures as photoanode materials show higher conversion efficiencies than the cells using their 1D trunk counterparts, there are still plenty room to enhance the cell efficiencies.

Herein, we describe the fabrication of the bunchy TiO_2 hierarchical structure consisting of 3D spheres stringed by the primary 1D nanobelt trunk. The modified fabrication processes enable the deposition of 3D integrated microspheres constructed by nanosheets, instead of individual nanosheets, on the 1D nanobelt trunk, which allows the novel bunchy TiO_2 spheres (BS-TiO_2) possessing the advantages both of the 3D architectures and the hierarchical architectures. It is demonstrated that the BS-TiO_2 based photoanode performs much better than the standard TiO_2 nanocrystalline (P25-TiO_2) based photoanode and the P25-TiO_2/scattering bilayer photoanode in the DSCs. In light of these results, it is concluded that photoanodes composed of BS-TiO_2 are attractive for solar cells, artificial photosynthesis, and other optoelectronic applications.

2. Results and discussion

To achieve fast electron transport, 1D nanobelt trunks with direct path for electron transport is selected. To get a large surface area for dye-loading and provide the light-scattering paths for light trapping inside the photoanode, it is rational to construct the micro-sized 3D integrated spherical structures with nanoscale building blocks. Hence, the architecture with spherical TiO_2 grown on nanobelt will increase effectively the light absorption and fast transport the photogenerated electrons collected by the nanoscale building blocks, leading to the high light harvesting efficiency and electron collection efficiency. A key problem in fabricating such TiO_2 structures is how to grow the integrated 3D spheres, other than nanoscale building blocks themselves, on the TiO_2 nanobelts. Hence, a modified template-free hydrothermal procedure with Ag cations as the agent and the TiO_2 nanobelts containing TiO_2-B phase was used for fabrication of such TiO_2 structures, the schematic processes of which are depicted in Fig. 1. The tetrabutyl titanate (TBOT) solutions with acetic acid ($C_2H_4O_2$) as the solvent were used in the reaction. In the typical procedure with TBOT and $C_2H_4O_2$ as the reactants (scheme 1), the product is typically amorphous. With the assistance of Ag cations and the fine adjusting of the content of Ag cations in the reaction solution (scheme 2), individual 3D spherical TiO_2 (S-TiO_2) constructed by ultra-thin nanosheets can be fabricated. In condition of the TiO_2 nanobelts with TiO_2-B as the surface crystalline phase presented in the reaction solution (scheme 3), the 3D spheres grow on the surface of the nanobelt, forming the bunchy spherical TiO_2 hierarchical structures (BS-TiO_2). It is worth noting that TiO_2-B phase in TiO_2 nanobelt is crucial for the growth of the 3D spheres on its surface, as TiO_2 nanobelt with pure anatase phase is not able to bunch the TiO_2 spheres.

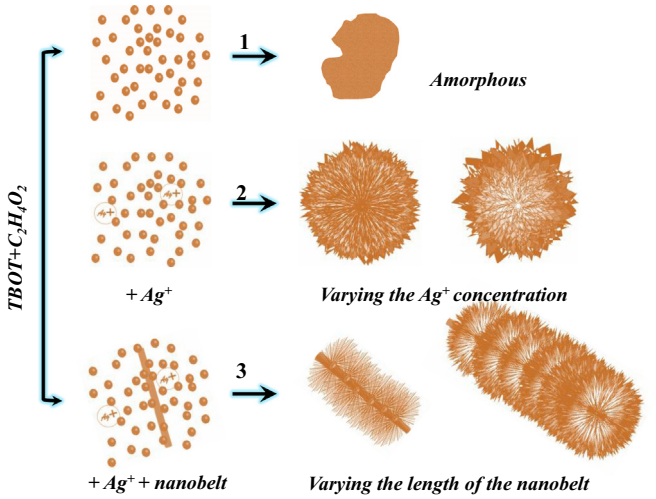

Fig. 1. Schematic illustration for the preparation of spherical TiO_2 (S-TiO_2) and bunchy spherical TiO_2 hierarchical structures (BS-TiO_2) from TBOT solutions with $C_2H_4O_2$ as the solvent.

Fig. 2 shows the typical SEM images of the products. The as-prepared S-TiO_2 shows the spherical morphology consisting of a large number of thin TiO_2 nanosheets; the outer diameter was approximately 2–4 μm (as shown in Fig. 2a–c). The density of the nanosheets on S-TiO_2 can be adjusted by varying the concentration and/or the ratio of Ag cations and the precursors. In the presence of TiO_2 nanobelt in the reaction solution, TiO_2 spheres integrated by nanosheets grow directly on the nanobelt, forming the bunchy spherical morphology. The outer diameter of BS-TiO_2 is approximate 1–2 μm, while its length is approximate 1–10 μm according to the length of inner TiO_2 nanobelt (Fig. 2d–f).

To further elucidate the microstructural features of the S-TiO_2 and BS-TiO_2 samples, transmission electron microscopy (TEM) were employed. Fig. 3a–b present the views of S-TiO_2 obtained from 100 $C_2H_4O_2$:1.15 TBOT: 0.12 $AgNO_3$. It is clear that S-TiO_2 is composite of ultra-thin TiO_2 nanosheets separated by nanoscale spaces. Fig. 3c shows the typical TEM image of the BS-TiO_2. The amplified TEM image (Fig. 3d) of BS-TiO_2 clearly reveals the growth of the spheres on the TiO_2 nanobelt.

The unique structure features of S-TiO_2 and BS-TiO_2 provide them large surface area. N_2 adsorption–desorption measurements evidence that the specific surface area (S_{BET}) of S-TiO_2 is around 172.7 m^2/g, which is two times larger than of standard P25 nanoparticles (59 m^2/g). BS-TiO_2 possesses an impressively high S_{BET} of 223.8 m^2/g (N_2 adsorption and desorption isotherms is shown in Fig. 4a), which is much higher than that of the reported quasi-1D hierarchical structures and 3D TiO_2 spheres (typically less than 100 m^2/g) [4,5,10,17,18], indicating the potential advantage of BS-TiO_2 for dye-adsorption in the photoanodes of the DSCs. The crystallinity and the phase property of the as-prepared BS-TiO_2 samples also benefit for the use in the photoanodes of DSCs, as revealed by the X-ray diffraction (XRD) patterns of the primary TiO_2 nanobelt and BS-TiO_2 shown in Fig. 4b. TiO_2 nanobelt shows the combination diffraction peaks of anatase phase and TiO_2-B phase. BS-TiO_2 after calcination at 600 °C shows the typical anatase phase, demonstrating the surface building blocks on the nanobelt, i.e. the 3D spheres, possess anatase phase. The anatase type of the 3D spheres is benefit for the use as the dye-loading matrix and electron acceptor in the photoanodes of DSCs [19].

Therefore, BS-TiO_2 with direct electron transport path and large specific surface area is selected to construct photoanodes in the DSCs. BS-TiO_2 and the standard P25-TiO_2 photoanodes were prepared by doctor-blading of BS-TiO_2 and P25-TiO_2 aqueous slurries, respectively, followed by calcination at 500 °C. Optical transmission spectra of BS-TiO_2 and P25-TiO_2 photoanodes are shown in Fig. 5a. The measurement was carried out using a spectrometer with an integrating sphere, taking into account the diffused light. BS-TiO_2 photoanode yields low transmittance, especially at the wavelength of 500–800 nm. Due to the large bandgap of TiO_2 (3.0–3.2 eV) [20], which only absorbs photons at the wavelength shorter than 410 nm, the reduced transmittance in BS-TiO_2 photoanode at long wavelengths can be ascribed to the effect of light

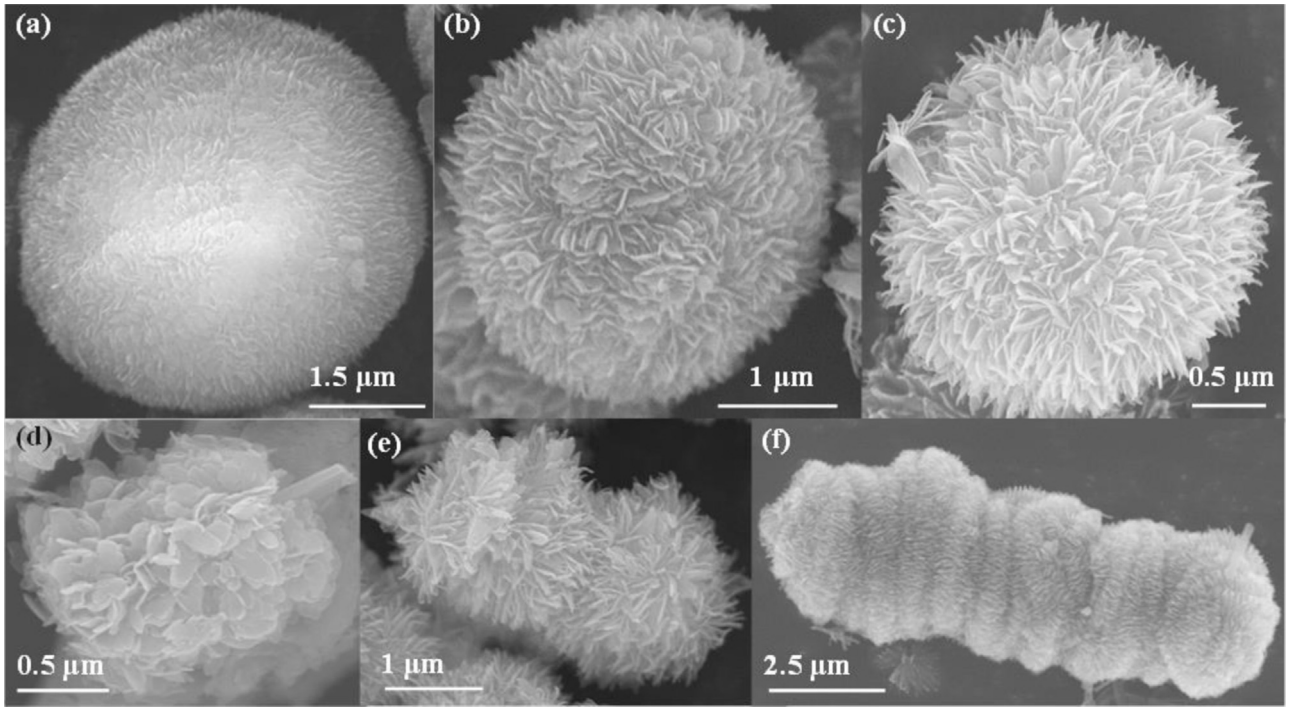

Fig. 2. (a–c) Scanning electron microscopy (SEM) images of S-TiO_2 with different surface morphologies obtained from TBOT solutions with $C_2H_4O_2$ as the solvent having the composition of (a) 100 $C_2H_4O_2$:2.3 TBOT: 0.95 $AgNO_3$, (b) 100 $C_2H_4O_2$:1.15 TBOT: 0.24 $AgNO_3$, and (c) 100 $C_2H_4O_2$:1.15 TBOT: 0.12 $AgNO_3$; (d–f) SEM images of BS-TiO_2 obtained from TBOT solutions having the composition of 100 $C_2H_4O_2$:1.15 TBOT: 0.12 $AgNO_3$ and 0.48 TiO_2 nanobelts with different lengths.

scattering inner BS-TiO_2 photoanode, as in accordance with the deduction from the morphology of BS-TiO_2. Considering the absorption spectrum of N719 dye (Fig. 5a), which has one main peak located at 510 nm, the light scattering effect in BS-TiO_2 photoanode will favors the light absorption of N719 in the photoanode. In addition, the amount of the adsorbed dye molecules is also increased due to the large specific surface area of BS-TiO_2. The dye-loading amount from BS-TiO_2 photoanode calculated by dye desorption is found to be 0.21 μmol/cm^2, which is much higher than that of P25-TiO_2 photoanode, as shown in Table 1. The favored light absorption and increased dye-loading will lead to increased light harvesting in the DSC with BS-TiO_2 photoanode.

Photocurrent–voltage (*J–V*) characteristics of the DSCs based on BS-TiO_2 and P25-TiO_2 photoanodes are shown in Fig. 5b. The photovoltaic parameters extracted from *J–V* curves are shown in Table 1. The DSC based on BS-TiO_2 photoanode shows the highest short-circuit photocurrent density (J_{SC}) of 14.3 mA/cm^2 and thus the highest power conversion efficiency (PCE) of 7.5%, which is 34% higher than these of DSC based on P25-TiO_2 photoanode (5.6%). Moreover, the DSC based on the bilayer photoanode including a P25-TiO_2 layer and a scattering layer composed by TiO_2 nanoparticles with the average diameter of 200 nm was also fabricated, and its photovoltaic parameters are shown in Fig. 5b and Table 1. The addition of the scattering layer to P25-TiO_2 photoanode has increased J_{SC} of the DSC to 13.9 mA/cm^2 and PCE to 7.1%, as in accordance with the enhanced light harvesting by the scattering layer, whereas these values are still lower than these obtained in the DSC based on a single layer of BS-TiO_2 photoanode. Hence, BS-TiO_2 possesses great potential in the application in the photoanode of the DSCs due to their optical and electron transport advantages.

To get an insight in the carrier transport property of the photoanodes, electrochemical impedance spectroscopy (EIS) is a powerful tool for interpreting the internal resistances and the electron transport phenomena within an electrochemical system [21,22]. EIS spectra of the DSCs with different photoanodes were carried out at the frequency range of 0.1 Hz to 100 kHz under one-sun illumination at V_{OC}. Fig. 6 shows Nyquist plots obtained from the DSCs based on BS-TiO_2 and P25-TiO_2 photoanodes. The spectra show three distinguishable arcs, which are associated with the charge transfer resistance (R_{ct1}) at Pt counter electrode, the recombination impedance at the TiO_2 photoanode (R_{ct2}) and the Warburg diffusion process of redox couple (Z_N) from the left to the right circle, respectively. The electron transport in the photoanode can be judged by the recombination impedance at the TiO_2 photoanode, which is estimated from the diameter of the middle semicircle by *Zview* software and listed in Table 2. The impedance is obviously small in BS-TiO_2 photoanode, which is agree with the speculation from its direct electron transport path. Accordingly, in the photoanode without direct electron transport path constructed by P25-TiO_2, the recombination impedance is larger. The different recombination impedances of the photoanodes are determined by the recombination dynamics in the photoanodes, which can be investigated by intensity-modulated photocurrent spectroscopy (IMPS) and intensity-modulated photovoltage spectroscopy (IMVS) measurements.

IMPS and IMVS measurements were performed to analyze the electron transport and recombination dynamics of the photoanodes. The electron transport time (τ_{tr}), the electron diffusion coefficient (D_n) and the electron recombination lifetime (τ_r) are determined from IMPS and IMVS measurements using the following schemes:

$$\tau_{tr} = 1/2\pi f_{min,IMPS} \quad (1)$$

$$D_n = d^2/C\tau_{tr} \quad (2)$$

$$\tau_r = 1/2\pi f_{min,IMVS} \quad (3)$$

Where $f_{min,IMPS}$ and $f_{min,IMVS}$ represent for the frequency minimum of imaginary part in IMPS and IMVS measurements, respectively; *d*

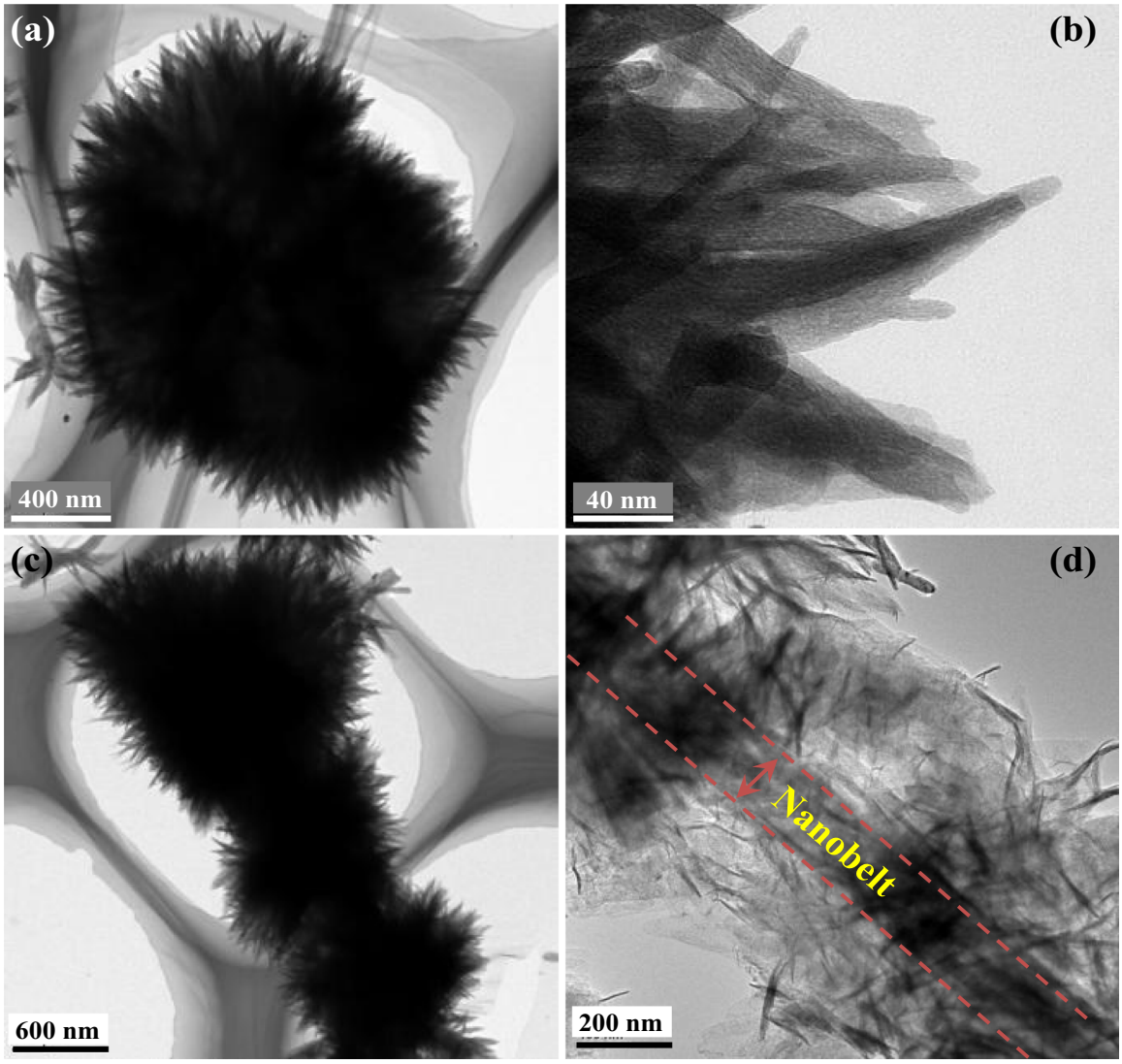

Fig. 3. TEM images of S-TiO_2 (a,b) and BS-TiO_2 (c,d) samples obtained from TBOT solutions with $C_2H_4O_2$ as the solvent having the composition of 100 $C_2H_4O_2$:1.15 TBOT: 0.12 $AgNO_3$.

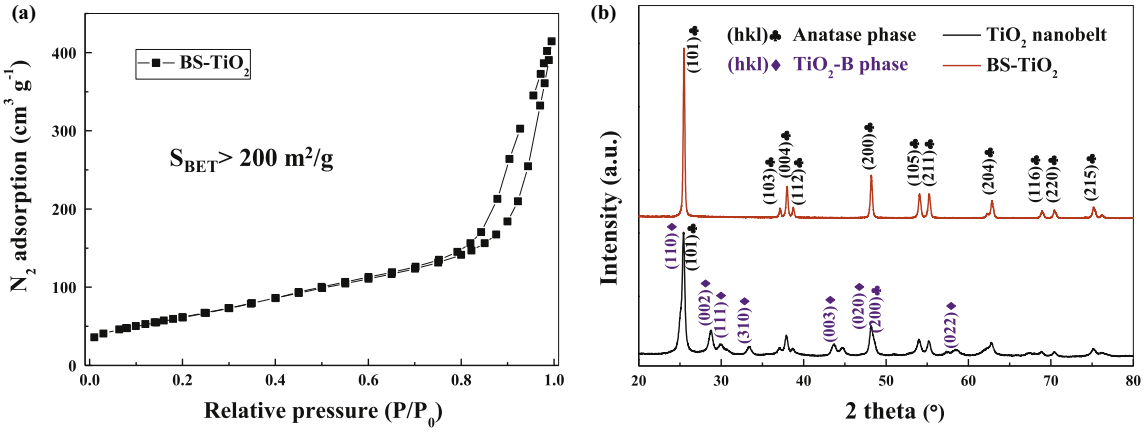

Fig. 4. (a) Nitrogen adsorption and desorption isotherms of BS-TiO_2 after calcinated at 350 °C; (b)XRD patterns of the TiO_2 nanobelt and BS-TiO_2.

represents for the thickness of the photoanode; C is a constant which equals to 2.5. Fig. 7 shows the D_n and τ_r values obtained from the IMPS and IMVS measurements, respectively, plotted as a function of the incident photon intensity. The highest electron diffusion coefficient was obtained from the BS-TiO_2 based cell, indicating that BS-TiO_2 photoanode is more efficient in transporting electrons than P25-TiO_2 photoanode. This can be ascribed to the direct electron transport path through the 1D nanobelt trunk. The TiO_2 nanobelt branch in BS-TiO_2 is efficient to shorten the electron transfer path and can easily collect electrons from

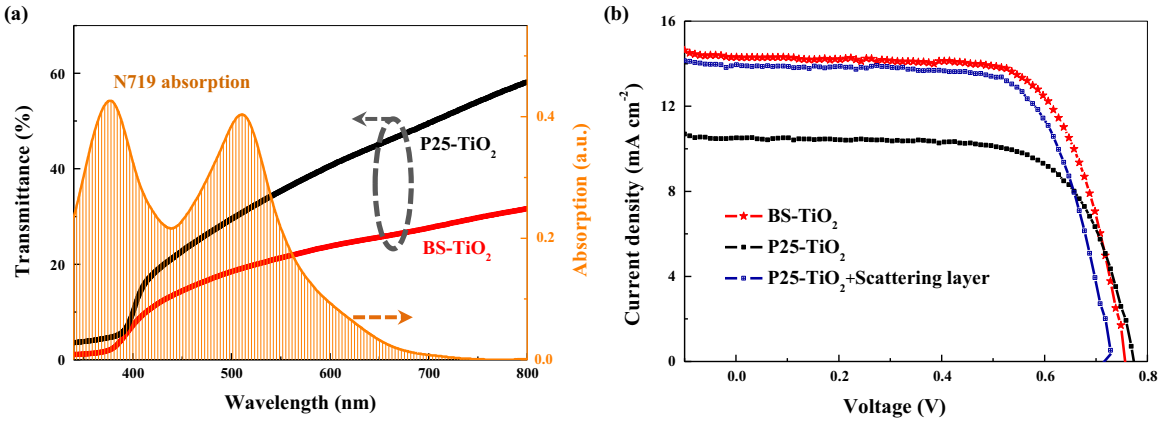

Fig. 5. (a) Transmittance spectra of the photoanodes fabricated with BS-TiO_2 and P25-TiO_2. (b) Photocurrent–voltage (J–V) curves of the DSCs using BS-TiO_2 and P25-TiO_2 photoanodes.

Table 1
Dye-loading amount of BS-TiO_2 and P25-TiO_2 samples and the corresponding photovoltaic parameters (J_{SC}, V_{OC}, FF, PCE) of the DSCs.

Samples	Dye-loading (μmol/cm^2)	V_{OC} (V)	J_{SC} (mA cm^{-2})	FF (%)	PCE (%)
BS-TiO_2	0.21	0.76	14.3	69	7.5
P25-TiO_2	0.08	0.77	10.5	69	5.6
P25-TiO_2+scattering layer	/	0.73	13.9	70	7.1

surface nanosheets, which improve the charge collection efficiency. On the other hand, the electron recombination lifetime of BS-TiO_2 photoanode is longer than that of P25-TiO_2 photoanode, despite of the much larger surface area of BS-TiO_2 which provides more trapping sites and leads to a larger charge recombination with I_3^- in the electrolyte. This can be attributed to the large grain size of BS-TiO_2 to establish efficient built-in potential for directing electron transport and reducing the surface recombination in BS-TiO_2 photoanodes.

The effective electron diffusion length (L_n) was obtained from $L_n = \sqrt{D_n \tau_r}$, which is the average distance an injected electron can travel through the photoanode prior to undergoing recombination. A long L_n is important for DSCs because only a small loss of injected charge occurs in the photoanodes with a longer L_n before it is collected. As shown in Table 2, the L_n of the BS-TiO_2 DSC is up to 37 μm, which is much higher than the P25-TiO_2 DSC, demonstrating the critical role of the nanobelt in electron transport. Furthermore, L_n of the BS-TiO_2 DSC is three times long of the optimal thickness (10–12 μm) of the photoanode, demonstrating that the generated electrons can reach the electrode with minor losses and thus, a much thicker film can be fabricated without negatively affecting the electron collection efficiency. Hence, further enhancement in the device efficiency can be achieved by optimizing the thickness of the photoanode based on BS-TiO_2.

The advantages of BS-TiO_2 are depicted in Fig. 8. In a DSC, as shown in Fig. 8a, the dye molecules in the photoanode absorb the incident light and TiO_2 in the photoanode transports the photogenerated electrons. In a typical photoanode using P25-TiO_2 and without scattering layer, as shown in Fig. 8b, the incident light travels across the photoanode without being scattered due to the nanoscale size of the nanoparticles. Meanwhile, the electron transport in P25-TiO_2 based photoanode lacks inherent directionality, and hence, the driving of electrons to a conductive contact for photocurrent extraction is not efficient. Thus, to balance

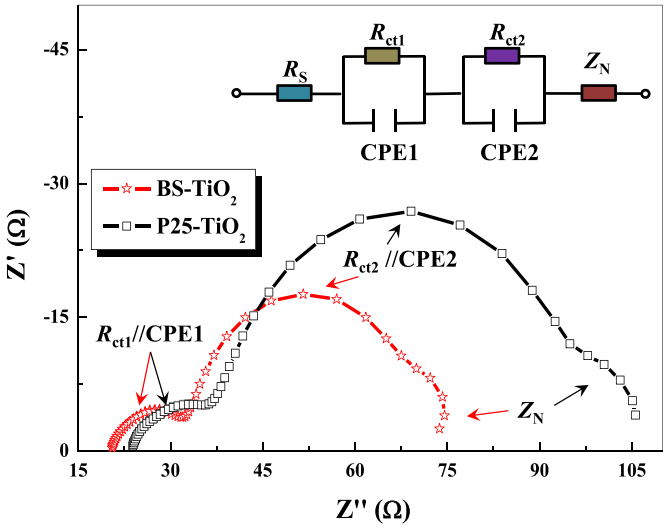

Fig. 6. EIS of DSCs based on different photoanodes. Inset shows the equivalent circuit of the DSCs. The irradiation intensity for measuring the J–V curves is 100 mW cm^{-2} under AM1.5 condition.

Table 2
The kinetic parameters determined from electrochemical measurements

Samples	R_{ct2} (Ω)	D_n (cm^{2}s^{-1})	τ_r (s)	L_n (μm)
BS-TiO_2	40	5.35*10^{-5}	0.25	36.8
P25-TiO_2	53	1.84*10^{-5}	0.07	11.3

the trade-off between the light harvesting and electron collection, typical P25-TiO_2 based photoanode yields moderate light and electron harvesting. A scattering layer is able to improve the light harvesting (Fig. 8b); however, the bilayer photoanode requires more complex fabrication processes and is not favorable for electron transport.

By replacing nanoparticulate films with quasi-1D architectures, i.e., BS-TiO_2 (Fig. 8c), the incident light can be scattered, which increases the optical path and thus the light harvesting efficiency. In addition, the enhanced light harvesting is also favored by the large surface area of BS-TiO_2 based photoanode for dye adsorption. Hence, single BS-TiO_2 layer is more efficient than P25-TiO_2/scattering layer in light harvesting. Furthermore, the photogenerated electrons are

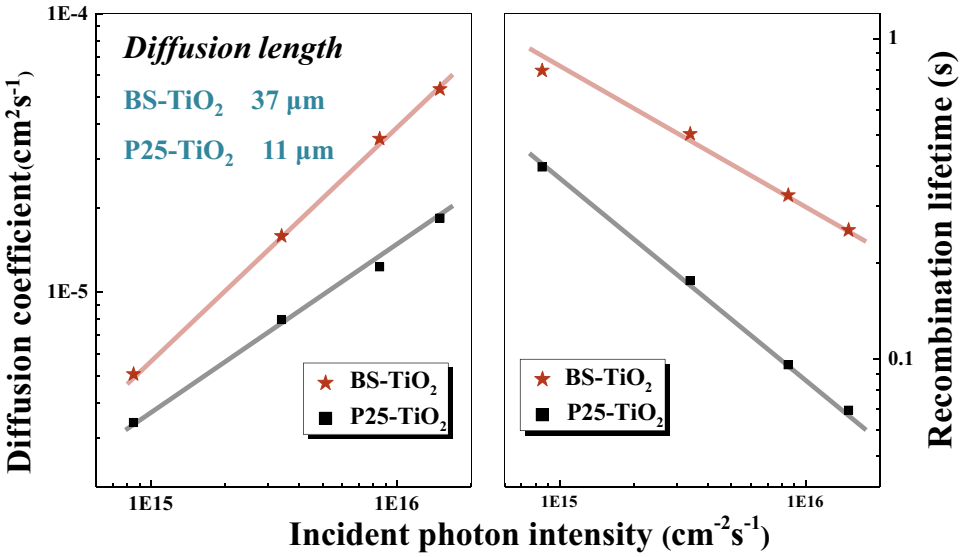

Fig. 7. Diffusion coefficient (D_n) and electron recombination lifetime (τ_r) of DSCs fabricated with different photoanodes, as determined from IMPS/IMVS measurements.

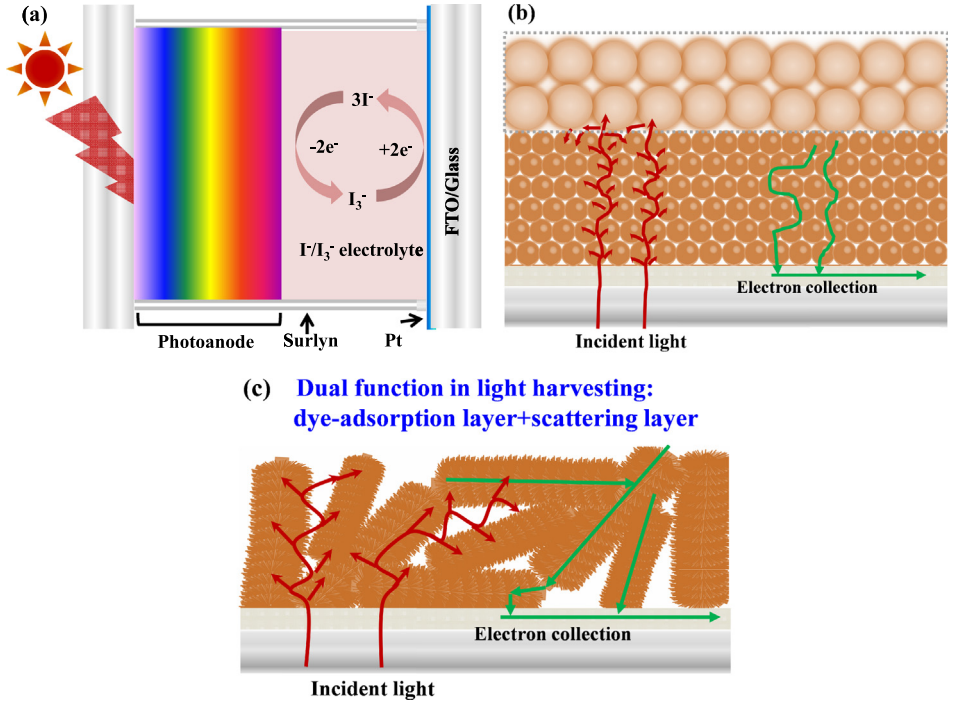

Fig. 8. (a) Schematic structure of a DSC; (b, c) Schematic mechanisms of the light transport and electron collection processes in different photoanodes, (b) P25-TiO_2 with and without scattering layer, and (c) BS-TiO_2.

allowed to move only in one dimension instead of randomly in three, leading to the much long diffusion length in BS-TiO_2 based photoanode. Hence, BS-TiO_2 photoanode can effectively improve the light harvesting and electron collection, leading to the enhanced photovoltaic performance of DSCs.

Hence, the excellent performance of the DSC using BS-TiO_2 photoanode is due to the increased light harvesting and electron collection through its large surface area for dye-loading, improved light scattering ability with their wavelength scale size and fast electron transport path through the 1D nanobelt. Furthermore, the unique properties of BS-TiO_2 with large specific surface area and fast electron transport also imply its great potential for the application in many fields including perovskite solar cells, photocatalytic and other optoelectronic devices.

3. Experimental

3.1. Fabrication of bunchy TiO_2 hierarchical structures

TiO_2 spheres were fabricated through hydrothermal synthesis with TBOT and acetic acid as the reactants and $AgNO_3$ as the agent [23]. Bunchy TiO_2 hierarchical spheres were obtained by introducing TiO_2 nanobelt [24] as the trunk in the synthesis of TiO_2 spheres. The concentration ratio of the reactants and $AgNO_3$ was varied to control the surface morphology of the TiO_2 structures.

3.2. Fabrication of DSCs.

TiO_2 photoanodes were prepared by doctor-blading of TiO_2 slurries on FTO/glass substrates. All of the TiO_2 photoanodes were

post-treated with $TiCl_4$. After calcination, TiO_2 photoanodes were immersed in 0.3 mmol/l ethanol solution of N719 dye for 24 h. DSCs were fabricated by assembling dye-sensitized TiO_2 photoanodes with sputtered Pt CEs [25] using 30 μm thick Surlyn. I^-/I_3^- electrolyte with acetonitrile as the solvent was used. Symmetric cells for electrochemical measurements were fabricated by assembling two identical CEs together using 30 μm thick Surlyn.

3.3. Characterization of the materials and DSCs

The structure and morphology of the materials were characterized by transmission electron microscopy (TEM, FEI Tecnai F20) and scanning electron microscopy (SEM, FEI Quanta 200F). Current density–voltage curves of DSCs were measured using a source meter (Keithley 2400) under AM 1.5 G irradiation with a power density of 100 mW/cm^2 from a solar simulator (XES-301S+EL-100). Electrochemical measurements were carried out using the electrochemical workstation (Zahner zennium) performed on DSCs under irradiation from solar simulator for EIS measurement and from light emitting diode (535 nm) for IMVS/IMPS measurements, respectively.

4. Conclusion

In conclusion, bunchy TiO_2 hierarchical spheres, consisting of 1D TiO_2 nanobelt and multiple TiO_2 microspheres constructed by nanosheets, were rationally designed and fabricated to enhance the light harvesting and electron collection in photoanodes of dye-sensitized solar cells. These bunchy TiO_2 hierarchical spheres exhibit faster electron transport properties and long electron diffusion length compared to TiO_2 nanoparticles. Moreover, they also show large specific surface area and improved light scattering. The excellent electron collection and light harvesting abilities of bunchy TiO_2 hierarchical spheres enable the enhancement of the conversion efficiency of the related solar cells. This work highlights the rational design of the TiO_2 nanostructures for highly efficient dye-sensitized solar cells, which also implies the application of the bunchy TiO_2 hierarchical spheres in other optoelectronic fields.

Acknowledgments

This work is supported partially by National High-tech R&D Program of China (863 Program, No. 2015AA034601), Natural Science Foundation of China (Grant nos. 91333122, 51402106, 51372082, 61204064 and 51202067), Ph.D. Programs Foundation of Ministry of Education of China (Grant nos. 20120036120006 and 20130036110012), Par-Eu Scholars Program, and the Fundamental Research Funds for the Central Universities.

References

[1] M. Grätzel, Acc. Chem. Res. 42 (2009) 1788–1798.
[2] B.E. Hardin, H.J. Snaith, M.D. McGehee, Nat. Photonics 6 (2012) 162–169.
[3] P.V. Kamat, K. Tvrdy, D.R. Baker, J.G. Radich, Chem. Rev. 110 (2010) 6664–6688.
[4] X. Sheng, D. He, J. Yang, K. Zhu, X. Feng, Nano Lett. 14 (2014) 1848–1852.
[5] S.H. Ahn, D.J. Kim, W.S. Chi, J.H. Kim, Adv. Mater. 25 (2013) 4893–4897.
[6] F. Sauvage, D. Chen, P. Comte, F. Huang, L.-P. Heiniger, Y.-B. Cheng, R.A. Caruso, M. Graetzel, ACS Nano 4 (2010) 4420–4425.
[7] D. Chen, F. Huang, Y.B. Cheng, R.A. Caruso, Adv. Mater. 21 (2009) 2206–2210.
[8] D. Chen, R.A. Caruso, Adv. Funct. Mater. 23 (2013) 1356–1374.
[9] L.P. Heiniger, F. Giordano, T. Moehl, M. Grätzel, Adv. Energy. Mater. 4 (2014).
[10] S.H. Ahn, D.J. Kim, W.S. Chi, J.H. Kim, Adv. Funct. Mater. 24 (2014) 5037–5044.
[11] X. Chen, X. Wang, X. Fu, Energy Environ. Sci. 2 (2009) 872–877.
[12] X.-Y. Li, L.-H. Chen, Y. Li, J.C. Rooke, C. Wang, Y. Lu, A. Krief, X.-Y. Yang, B.-L. Su, J. Colloid Interface Sci. 368 (2012) 128–138.
[13] Y. Li, Z.Y. Fu, B.L. Su, Adv. Funct. Mater. 22 (2012) 4634–4667.
[14] J. Kim, H. Lee, D.Y. Kim, Y. Seo, Adv. Mater. 26 (2014) 5192–5197.
[15] J.H. Pan, X.Z. Wang, Q. Huang, C. Shen, Z.Y. Koh, Q. Wang, A. Engel, D. W. Bahnemann, Adv. Funct. Mater. 24 (2014) 95–104.
[16] L. Passoni, F. Ghods, P. Docampo, A. Abrusci, J. Martí-Rujas, M. Ghidelli, G. Divitini, C. Ducati, M. Binda, S. Guarnera, ACS Nano 7 (2013) 10023–10031.
[17] Z. Sun, J.H. Kim, Y. Zhao, F. Bijarbooneh, V. Malgras, Y. Lee, Y.-M. Kang, S.X. Dou, J. Am. Chem. Soc. 133 (2011) 19314–19317.
[18] J.B. Joo, M. Dahl, N. Li, F. Zaera, Y. Yin, Energy Environ. Sci. 6 (2013) 2082–2092.
[19] N.-G. Park, J. Van de Lagemaat, A. Frank, J. Phys. Chem. B 104 (2000) 8989–8994.
[20] D.O. Scanlon, C.W. Dunnill, J. Buckeridge, S.A. Shevlin, A.J. Logsdail, S. M. Woodley, C.R.A. Catlow, M.J. Powell, R.G. Palgrave, I.P. Parkin, Nat. Mater. 12 (2013) 798–801.
[21] D. Song, M. Li, Y. Li, X. Zhao, B. Jiang, Y. Jiang, ACS Appl. Mater. Interfaces 6 (2014) 7126–7132.
[22] Q. Wang, J.E. Moser, M. Gratzel, J. Phys. Chem. B 109 (2005) 14945–14953.
[23] Y. Jiang, M. Li, D. Song, X. Li, Y. Yu, J. Solid State Chem. 211 (2014) 90–94.
[24] W. Zhou, Z. Yin, Y. Du, X. Huang, Z. Zeng, Z. Fan, H. Liu, J. Wang, H. Zhang, Small 9 (2013) 140–147.
[25] D. Song, P. Cui, X. Zhao, M. Li, L. Chu, T. Wang, B. Jiang, Nanoscale 7 (2015) 5712–5718.